Nano Research 2013, 6(1): 55–64
DOI 10.1007/s12274-012-0281-7
Research Article

ISSN 1998-0124
CN 11-5974/O4

Flexible SnS nanobelts: Facile synthesis, formation mechanism and application in Li-ion batteries

Jun Lu[1,2], Caiyun Nan[1,2], Lihong Li[1,2], Qing Peng[1,2] (✉), and Yadong Li[1,2]

[1] *Department of Chemistry, Tsinghua University, Beijing 100084, China*
[2] *State Key Laboratory of Low-Dimensional Quantum Physics, Tsinghua University, Beijing 100084, China*

Received: 25 September 2012
Revised: 21 November 2012
Accepted: 26 November 2012

KEYWORDS
tin sulfide,
nanobelts,
Li-ion battery,
morphology preservation

ABSTRACT

[020]-oriented tin sulfide nanobelts with a length/thickness ratio of 100 have been synthesized by a facile hydrothermal method without any surfactants, and the nanobelts have shown good strain-accommodating properties as well as good electrochemical performance as the anode for Li-ion batteries. The formation of the nanobelts results from a precipitation–dissolution–transformation mechanism, and the [020] oriented growth can be ascribed to the {010} facet family having the lowest atomic density. In particular, SnS shows clear Li–Sn alloying/de-alloying reversible reactions in the potential range 0.1–1.0 V. Based on galvanostatic measurements and electrochemical impedance spectroscopy, SnS nanobelts have shown impressive rate performance. The post-cycled SnS nanobelts were completely transformed into metallic tin, and preserved the one-dimensional structure due to their flexibility which accommodates the large volumetric expansion.

1 Introduction

Orthorhombic tin(Ⅱ) sulfide has become increasingly attractive because of its potential for a wide range of applications including Li-ion batteries, solar cells, near-infrared detectors, and thermoelectric devices [1–6]. The merits of SnS, which meet increasing practical, economic and environmental concerns, include its ultra-high capacity which reaches 780 $mA \cdot h \cdot g^{-1}$, cheapness, abundance and stability, adding up to a great potential for use as the anode material of Li-ion batteries [7–11]. Specifically, SnS is also capable of high charge–discharge rates in high power Li-ion batteries because of its intrinsic high electrical conductivity of 0.193 to 0.0083 $S \cdot cm^{-1}$ [5, 12]. However, the large volumetric expansion of SnS caused by Li–Sn alloying process results in pulverization and rapid, severe capacity fade [13, 14].

One-dimensional (1D) nanomaterials have been intensively investigated for Li-ion batteries due to their flexibility, one-dimensional pathway for electron transport, as well as large surface area [15–21]. The enhanced structural stability and capacity preservation of 1D nanomaterials has been demonstrated for SnO_2 nanowires [15], Si nanowires [16], and Fe_2O_3 nanotubes [17]. Furthermore, the rate capability of 1D

Address correspondence to pengqing@mail.tsinghua.edu.cn

nanomaterials also has been found to be greatly improved compared to other forms of the same materials, including $LiMn_2O_4$ nanorods and nanowires [18, 19], $LiFePO_4$ nanowires [20], and $LiCoO_2$ nanotubes [21]. Therefore 1D nanostructures of SnS could exhibit unique electrochemical properties for Li-ion batteries. Recently, 1D nanostructures of SnS including short nanobelts, nanowires and nanorods have been obtained by a solvothermal method [22], and a surfactant assisted approach [23, 24]. However, facile synthetic approaches have rarely been reported, and investigations of 1D SnS nanostructures on electrochemical properties have only been briefly mentioned.

Herein, flexible, [020] oriented SnS nanobelts 11 μm in length, 500 nm in width and 100 nm in thickness have been synthesized without any surfactants, and the rate performances as well as other electrochemical properties of the nanobelts were examined when used as the anode material for Li-ion batteries. The hydrothermal method has been employed for the synthesis of SnS nanobelts, and is facile and easy to scale up. As a result of investigating the influence of varying hydrothermal reaction times, the precipitation–dissolution–transformation (PDT) mechanism has been proposed as the growth process of the nanobelts. For the electrochemical properties of the SnS nanobelts, cyclic voltammetry shows the irreversible displacement reaction of SnS to Sn and Li_2S above 1.0 V, and reversible Li–Sn alloying reaction below 1.0 V. The 1D nanomaterial has a sound rate capability during the electrochemical measurements and the capacity fade has been found to be related to the formation of inactive Li–Sn alloys, and the increasing polarization resistance caused by the solid electrolyte interface (SEI). It is emphasized that the flexible nanobelts preserve the 1D structure after cycling, showing their excellent tolerance for volumetric expansion. In addition, the SnS nanobelts also exhibit unique photon absorption properties in that a high absorbance is maintained from the ultraviolet to the near-infrared region.

2 Experimental

2.1 Synthesis of SnS nanobelts

$SnCl_2{\cdot}2H_2O$, $CO(NH_2)_2$ (urea) and CH_3CSNH_2 (TAA) were purchased from China National Medicines Corp., L. T. D. Urea was employed to adjust the pH. For a typical synthesis, 10 mmol of urea and 10 mmol of TTA were dissolved in 40 mL of water with stirring, and 0.6 mmol of $SnCl_2{\cdot}2H_2O$ was added. After further stirring for 5 min, the solution was transferred into an autoclave and kept at 170 ˚C for 10 h. The silver gray product obtained at the bottom of the autoclave was washed several times with deionized water and dried in a 70 ˚C oven.

2.2 Characterization

The X-ray diffraction (XRD) patterns of the samples were collected on Bruker D8 Advance X-ray powder diffractometer with Cu Kα radiation (λ = 0.154056 nm) in the 2θ range 10° to 70°. The Fourier transform infrared (FT-IR) spectra of the sample were collected on a PerkinElmer Spectrum GX from 4000 to 450 cm^{-1}. The morphologies were characterized using a field-emission transmission microscope (FESEM) (LEO-1530) and the elemental composition of the material was determined by energy-dispersive X-ray spectroscopy (EDS) (Oxford 7426 attached to the FESEM) at the voltage of 20 kV. High-resolution transmission electron microscopy (HRTEM) was also performed using a FEI Tecnai G2 F20 S-Twin microscope working at an acceleration voltage of 200 kV. Absorption spectra were recorded on a UV-3600 UV–vis–NIR spectrophotometer (Shimadzu, Japan).

2.3 Electrochemical measurements

SnS material was fabricated into CR2016 coin-type cells for electrochemical tests. Blends of active material, acetylene black and polyvinylidene difluoride (PVDF) in the mass ratio of 6:2:2 were well ground and pasted on copper foil. After drying in a 120 ˚C vacuum oven for 12 h, the material was fabricated into coin-type cells in an Ar-filled glove box using lithium metal as the counter electrode, Celgard 2300 membrane as the separator and 1 M $LiPF_6$ solution in dimethyl carbonate/ethylene carbonate (DMC/EC) (1:1 by volume) as the electrolyte. The rate and cycling examinations were carried out on battery testing system (BTS-5 V 5 mA, Neware) in the voltage range 3.0–0.1 V. A CHI 660D electrochemical station was

employed for the cyclic voltammetry (CV) in which the voltage was varied from 3.0–0.1 V with a scanning rate of 0.1 mV·s^{-1}, and electrochemical impedance spectroscopy (EIS) with the frequency range of 10 kHz to 2.5 Hz and magnitude of the alternative signal of 10 mV.

3 Results and discussion

3.1 Structure and morphology of SnS nanobelts

The XRD pattern of SnS nanobelts is presented in Fig. 1(a). All peaks of the nanostructure can be well matched with the peaks of standard orthorhombic SnS (JCPDS card No. 73-1859) with lattice constants a = 1.118 nm, b = 0.3982 nm and c = 0.4329 nm, showing that the product is phase-pure orthorhombic tin(II) sulfide. The intensity of the peak at 2θ = 32.06° indexed as (400) is significantly enhanced compared with that for the standard sample, showing that the SnS product mostly has exposed facets of the {100} family. EDS (Fig. S1 in the Electronic Supplementary Material (ESM)) gave an atomic Sn:S ratio of 50.8:49.2 confirming the purity of the product SnS. As the SnS nanobelts were synthesized in a system containing NH_4^+, HS^- and CH_3COO^- ions, it is important to determine whether any such species were adsorbed on the surface of the nanobelts. The FT-IR spectrum of the washed SnS product is shown in Fig. 1(b). For the purpose of better detecting any adsorbed species, the SnS:KBr ratio in the disk was higher than normal. The transmittance curve shows that the SnS material is free of NH_3, NH_4^+, HS^- or CH_3COO^- absorptions, and only H_2O, giving rise to peaks at 3500 and 1620 cm^{-1}, is present [23]. The FT-IR suggests that the above-mentioned adsorbents do not have a strong coordination interaction with the SnS surface, and thus these absorbents can be assumed not to have an important role in the growth process of the SnS nanostructure.

The oriented morphology of product is confirmed by the SEM images in Figs. 1(c) and 1(d). The SnS nanostructure which has a rectangular morphology with clear edges has typical length/thickness and thickness/width ratios of approximately 100 and 5

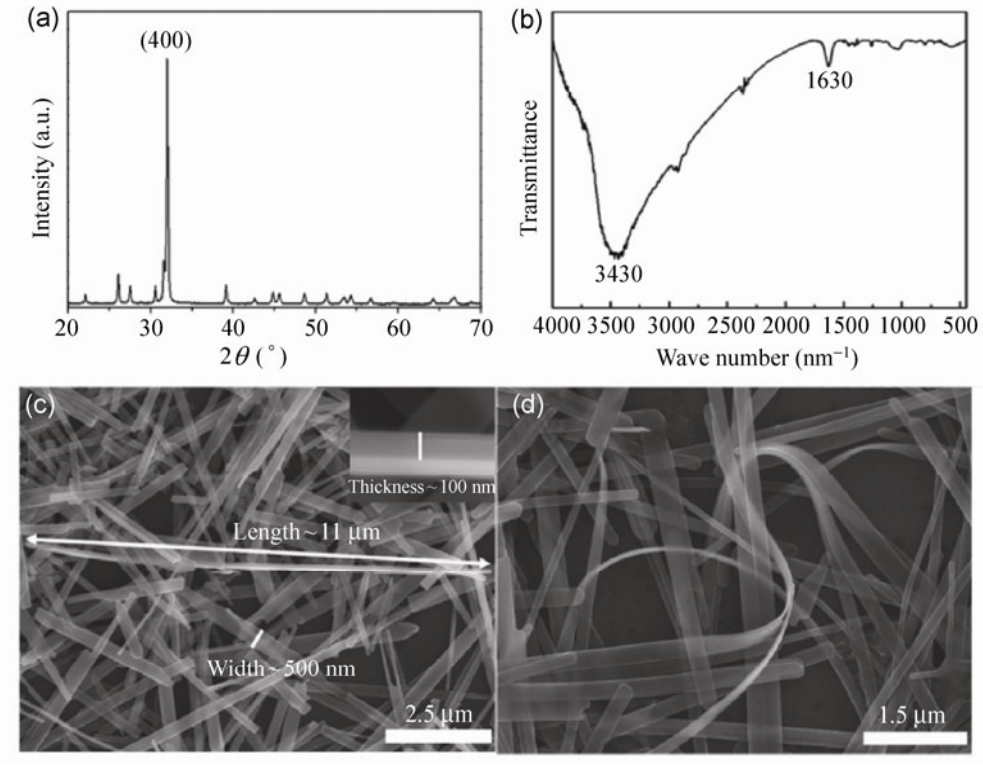

Figure 1 X-ray diffraction pattern (a), FT-IR spectrum (b) and SEM images (c) and (d) of the SnS nanomaterial. In the FT-IR spectrum, the minor peaks around 2900 and 2400 cm^{-1} are ascribed to contaminants in the FT-IR spectrometer.

respectively, demonstrating that the SnS material has a nanobelt morphology. In Fig. 1(d), the nanobelts with the thickness of 50 nm have been bent, indicating the flexibility of the 1D nanostructure.

The HRTEM image shown in Fig. 2(a) further confirms the nanobelt structure. It can be seen that the nanobelts are mainly lying on the carbon membrane support. The ripple-like fringes are probably caused by the strain due to bending and twisting of the nanobelt, which is characteristic for 1D and 2D nanostructures [11, 22]. Also, the width of nanobelts ranges from 80–300 nm, consistent with the SEM observations. Figure 2(b) shows the HRTEM image of the lateral face of a SnS nanobelt. The indexed selected area electron diffraction (SAED) pattern is shown in the insert of Fig. 2(b). The clear diffraction spots indicate that the nanobelts are single crystalline. It can be seen that the nanobelts grow along [020] direction which is the same as for other nanobelts, and the lateral facet of the nanobelts belongs to the family of {100} planes. This is consistent with the significant enhancement of the (400) peak in the XRD pattern.

As the surfaces of SnS nanobelts are free of adsorbed species, the differences in surface energies and atomic densities for given crystal facets of SnS are important for the oriented growth. Actually, the growth orientation of SnS nanobelts can be explained

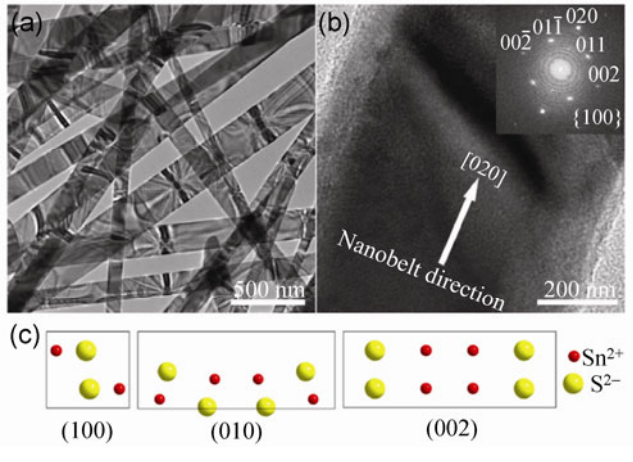

Figure 2 HRTEM image of SnS nanobelts (a), selected HRTEM image of the lateral facet of the belt with SAED obtained by Fourier fast transformation (FFT), and the ionic arrangement of the (100), (010) and (002) facets of SnS (c).

by surface energy theory, considering the anisotropic features of the SnS crystal structure [25]. The surface energy theory depicts that the exposed surface of high-energy facets will be minimized and that of low-energy facets will be maximized so that the total surface energy is minimized. In the case of the orthorhombic structure of SnS with a = 1.182 nm, b = 0.399 nm and c = 0.434 nm, the surface energies of the {100}, {010} and {001} facet families are closely related to the ionic arrangements. The most dense facet for {100}, {010} and {001} facet families are (100), (010) and (002) facets, respectively, which are shown in Fig. 2(c); the surface densities of Sn–S ion pairs are calculated to be 11.5, 7.8 and 8.3 nm^{-2} respectively. This indicates that the (100) and (010) facets, with the most and least dense ion arrays, respectively, are the most and least stable facets due to the strongest and weakest ionic interactions, respectively. Accordingly, it is rational that the SnS nanostructure tends to expose (100) facets, and the (010) facets which are weakly dominated by (002) facets are the least exposed facets of the crystal. As a result, the preferred growth direction is the [020] direction. This analysis is consistent with the XRD and HRTEM observations.

3.2 Formation mechanism

By investigating the growth process of SnS nanobelts by varying the elapsed time for hydrothermal treatment, a growth mechanism for the SnS nanobelts has been proposed. The SEM images in Fig. 3 are for materials synthesized with reaction times of 0, 2, 8 and 10 h. The XRD patterns (Fig. S2 in the ESM) show that the samples obtained after 0 and 10 h are zinc blende (ZB), and orthorhombic SnS respectively, which indicates that a phase transformation from ZB to orthorhombic SnS had occurred in the process. For the hydrothermal process, the hydrolysis reaction in Eq. (1) will occur first, and then HS^- ions and Sn^{2+} ions will react immediately to precipitate SnS shown as Eq. (2). Urea was employed to adjust the pH value of the solution since this is important to control the growth rate of the SnS [26].

$$CH_2CSNH_2 + CO(NH_2)_2 + 4H_2O \rightarrow 3NH_4^+ + HCO_3 + HS \quad (1)$$

$$Sn^{2+} + HS^- + HCO_3^- \rightarrow SnS + H_2CO_3 \quad (2)$$

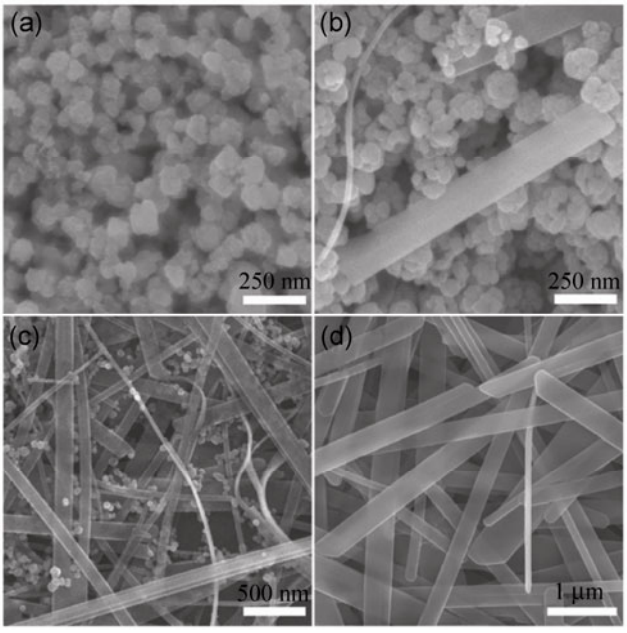

Figure 3 SnS nanomaterials obtained with reaction times of 0 h (a), 2 h (b), 8 h (c), and 10 h (d).

When the time for hydrothermal reaction was prolonged, the morphologies of the samples evolved from spherulitic nanoparticles with a diameter of about 100 nm (0 h), to a mixture of nanoparticles and nanobelts (2–8 h), and finally to pure nanobelts (10 h). Due to the supersaturation and fast nucleation of SnS in the initial solution, spherulitic SnS nanoparticles indexed as NaCl-type SnS were formed as the initial precipitate. Similar to its polymorph zinc blende ZnS, the NaCl-type SnS is metastable under the hydrothermal conditions [27, 28]. In the subsequent steps, metastable SnS nanoparticles dissolved into aqueous Sn^{2+} and HS^- ions, which then adsorbed selectively onto the thermodynamically unfavoured (010) and (002)facets of orthorhombic SnS, leaving {100} facets as the major exposed facets. During the growth process, the [020] direction is the most favored due to its least dense atomic arrangement. As a result, the SnS nanostructure grows along the [020] direction and nanobelts are finally obtained. Different from the mechanism of decomposition–aggregation–growth in the literature [29], the phase and morphology evolutions showed that the growth mechanism of orthorhombic SnS nanobelts follows a PDT process shown in Eq. (3) and Scheme 1.

$$SnS_{(ZB)} + H_2O \rightarrow Sn^{2+} + HS^- + OH^- \rightarrow SnS_{(OR)} + H_2O \quad (3)$$

3.3 Applications of SnS nanobelts

The UV–vis–NIR absorption spectrum of the SnS nanobelts is shown in Fig. 4(a). The SnS nanobelts have a strong, broad absorption ranging from the ultraviolet to the near-infrared. Specifically, the nanobelts show a gradually increasing absorption with increasing photon energy in the near-infrared region. In the range 390–800 nm, the absorption stays relatively stable, and shows a broad peak around 768 nm. The nanobelts have much better photon absorption properties than other SnS materials reported in the literature [29–31], which indicates the potential of the nanobelts for use in solar energy conversion and near-infrared detectors.

Cyclic voltammetry characterization was carried out by the two-electrode method employing lithium as the counter and reference electrode in the voltage range 0.1–3 V with a scanning rate of 0.1 $mV \cdot s^{-1}$ at room

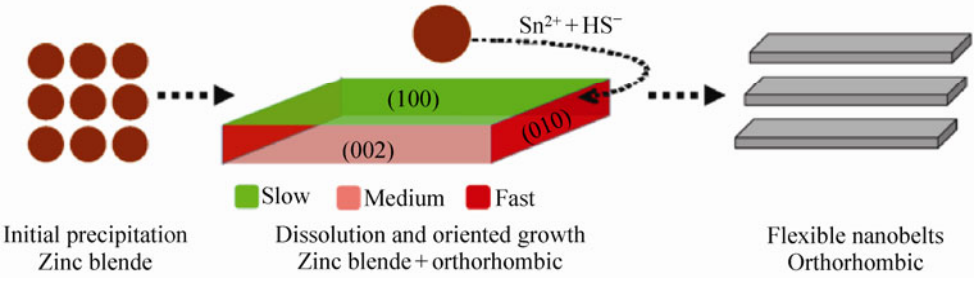

Scheme 1 PDT mechanism of SnS nanobelts. The (100), (010) and (002) facets with different atomic densities are shown in gray, green and red colors, respectively.

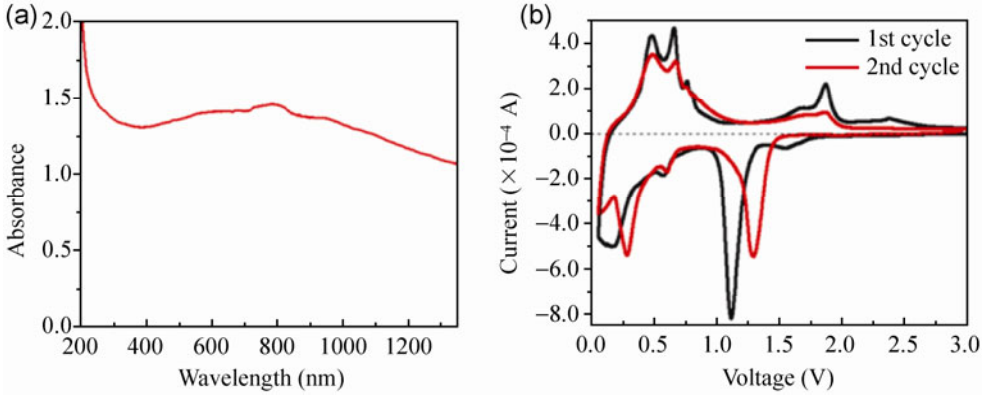

Figure 4 UV–vis–NIR absorption of SnS nanobelts in the range 200 to 1350 nm (a). Cyclic voltammetry of SnS nanobelts from 3.0–0.1 V with a scanning rate of 0.1 $mV \cdot s^{-1}$ (b).

temperature (Fig. 4(b)). The peaks for discharging and charging potentials are listed in the Table 1. The peaks above 1.0 V correspond to the displacement reaction of Li and SnS which is shown in Eq. (4), and similar results have previously been reported for SnO_2 and SnS_2 [15, 32–34].

$$SnS + 2Li^+ + 2e^- \rightarrow Li_2S + Sn \quad (4)$$

It can be seen that the I_{pc} is much smaller than I_{pa}, and the potential difference (0.76 V) between E_{pa} and E_{pc} in the first cycle is much larger than the theoretical value of 0.057 V for a reversible reaction at 287 K, indicating that this reaction is irreversible [34]. In addition, the peak currents for the reaction in the first and second cycle are 817 and 544 μA for reduction of SnS, and 222 and 95 μA for oxidation of Sn respectively.

Table 1 Peak potentials and currents of SnS nanobelts (versus Li metal) in the cyclic voltammetry curves

	No.	1st cycle		2ed cycle	
		E (V)	I (μA)	E (V)	I (μA)
Negative scan	1	1.11	817	1.29	544
	2	0.568	185	0.597	168
	3	0.156	500	0.277	537
Positive scan	4	0.479	434	0.478	352
	5	0.656	466	0.672	321
	6	0.762	235	0.761	207
	7	1.87	222	1.87	95

For the peaks below 1.0 V, the alloying reaction between Li and Sn shown in Eq. (5) takes place.

$$Sn + xLi^+ + xe^- \rightarrow Li_xSn \quad (5)$$

The potential of Li_xSn varies with the content of lithium in the Li–Sn alloy. For the first cycle, the weak peak at 0.568 V can be assigned to the alloying process of Li_xSn with the x range of 0.57–1.0 [35]. When the potential decreased, the current increased continuously, with the maximum I_{pa} at $E_{pa} = 0.156$ V, which can be assigned to the overlap of discrete lithium alloying processes within the lithium content range (x) of 1.0–4.4 [35]. In the positive scanning curve, the de-alloying processes separated into three individual peaks, showing the discrete nature of the alloying and de-alloying processes. For the second cycle, similar results were found except for the positive-shifted peak at $E_{pa} = 0.277$ V, which could be the result of electrochemical activation of the material during the first cycle. Although the alloying process is reversible, the corresponding oxidation and reduction peaks are unclear, which makes further analysis of the I_{pa} and I_{pc} data somewhat difficult.

SnS nanobelts were cycled under currents from 1/6 C to 5/3 C, and the capacity profiles and discharge–charge curves are presented in Figs. 5(a) and 5(b) respectively. The initial capacity of SnS at 1/6 C is 1226 $mA \cdot h \cdot g^{-1}$, which is larger than the theoretical initial capacity of SnS (1138 $mA \cdot h \cdot g^{-1}$) due to the side reactions. The value is comparable with those for SnO_2

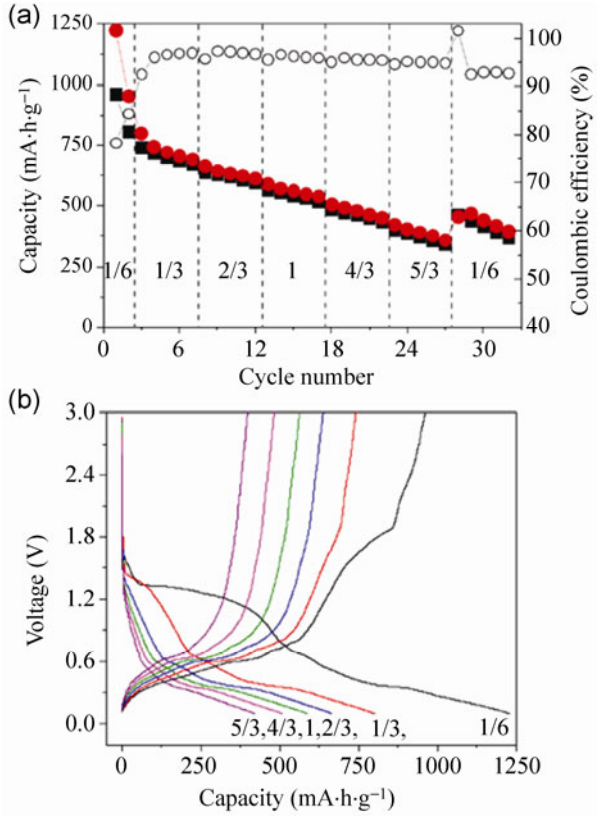

Figure 5 Rate performance (a) and voltage profiles (b) of SnS nanobelts under various charge–discharge rates (1 C = 750 mA·g^{-1}).

and SnS_2 materials [32, 36]. The average capacities under elevated currents are 1091, 734, 636, 562, 478, 390 mA·h·g^{-1}, and the capacity returned to 436 mA·h·g^{-1} for the final 1/6 C cycling, giving 94% coulombic efficiency. It should be noted that the capacity fade can be regarded as not strongly dependent on the increase in rate, since the capacity drops for each current increase are difficult to distinguish. This indicates that the SnS nanobelts are capable of high rate performance, while the capacity stability is disadvantageous for practical application where further improvement is needed. Figure 5(b) shows that the voltage plateau for discharging is at 1.30 V, which only can be seen in the first cycle corresponding to the displacement reaction. This is in good agreement with the CV curve. The Li–Sn alloying process taking place below 0.6 V decreases with increasing current density, which could be the main reason for the capacity fade. To further investigate the capacity fade, a deep analysis of the charge–discharge capacity data and EIS has been carried out.

The Nyquist plots of the SnS nanobelts before and after cycling, with the different equivalent circuits, are presented in Fig. 6(a) and the resistance data are given in Table 2. It can be seen that the nanomaterial behaved quite differently before and after cycling. The most obvious difference is that a polarization circuit consisting of R_p and CPE_p appeared after cycling, which can be ascribed to the side reaction–which is referred as a solid electrolyte interface (SEI) in the literature–and the presence of amorphous Li_2S on the material, which both cause polarization [13, 35, 37]. A dramatic decrease in R_{ct} is also noticed, and could be the result of the better electronic conductivity of metallic tin. Detailed fitting results of the equivalent circuit, with tolerable errors (<10%), are available in Table S1 (in the ESM).

Table 2 Resistances of the equivalent circuit obtained for different states of the battery

	R_s (Ω)	R_p (Ω)	R_{ct} (Ω)
Initial state	7.65	–	110.30
Final state	5.94	3.96	16.62

To understand the phase and morphology changes of the material caused by cycling, XRD and SEM characterization was carried out on the anode blend after the rate test. The XRD pattern in Fig. 6(b) shows that the SnS has been transformed into metallic tin during the cycling, which is consistent with the proposed reaction mechanism. No peaks characteristic of crystalline Li_2S are found, indicating that the Li_2S is amorphous rather than crystalline. These observations are also in accordance with the literature for SnS [14] and the data for tin oxide composites [38]. In Fig. 6(c), the cycled nanomaterials have expanded in thickness and width, and the surfaces of the nanobelts have become rough. However, the material clearly preserves the nanobelt morphology. As mentioned above, the volumetric change of the material during the Li–Sn alloying process has been reported and is regarded as one of reasons for the pulverization of tin-based materials, and the deterioration of the electrode

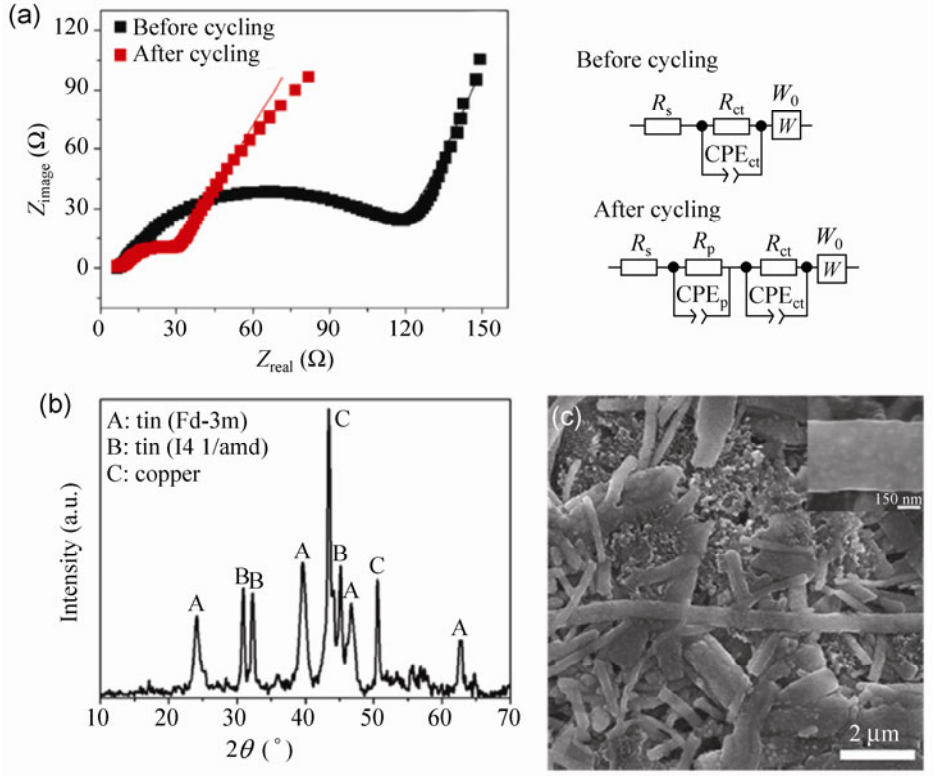

Figure 6 Nyquist plots of batteries corresponding to the initial and final state with the equivalent circuit (a). XRD (b) and SEM (c) images of post-cycled SnS nanobelts. The insert in the SEM image is the magnified image of electrochemically cycled SnS nanobelts.

contact [13, 33, 38, 39]. In the case of SnS nanobelts, the preservation of the morphology is unexpected, and could be a result of the unique flexibility of the 1D structure. This observation indicates that the SnS nanobelts could have potential for better electrochemical performance than other SnS materials.

4 Conclusions

One-dimensional SnS nanobelts have been synthesized by a facile hydrothermal method without any surfactants. They grow along the [020] direction and expose (100) facets, owing to the anisotropic atomic arrangements on the (100), (010) and (002) planes. By following the effects of varying the synthesis parameters, the growth of the nanobelts has been suggested to follow a precipitation–dissolution–transformation mechanism. The electrochemical properties have been investigated by cyclic voltammetry, rate tests and electrochemical impedance spectroscopy. The CV method shows the reversible Li–Sn alloying reaction is combined with an irreversible displacement reaction of SnS to afford Sn and Li_2S. In the rate test, the nanobelts show good rate capability, as well as a relatively high coulombic efficiency of 94%. The cycled SnS nanobelts became fully transformed into metallic tin and preserved the 1D structure owing to the flexibility and structural stability of the 1D nanobelts. In addition, SnS nanobelts have unexpected strong photon absorption properties spanning the ultraviolet to the near-infrared region.

Acknowledgements

This work was supported by the State Key Project of Fundamental Research for Nanoscience and Nanotechnology (Nos. 2011CB932401 and 2011CBA00500), and the National Natural Science Foundation of China (Nos. 20921001 and 21051001). We are grateful to Associate Professor Jiaping Wang and lab assistant Fei Zhao in the Tsinghua–Foxconn Nanocenter for their generous help in the fabrication of batteries.

Electronic Supplementary Material: Supplementary material (EDS spectrum of SnS nanobelts, XRD patterns of SnS with reaction time of 0 and 10 h, detailed EIS fitting data for the SnS nanobelts before and after cycling) is available in the online version of this article at http://dx.doi.org/10.1007/s12274-012-0281-7.

References

[1] Sharon, M.; Basavaswaran, K. Photoelectrochemical behaviour of tin monosulphide. *Solar Cells* **1988**, *25*, 97–107.

[2] Price, L. S.; Parkin, I. P.; Hardy, A. M. E.; Clark, R. J. H.; Hibbert, T. G.; Molloy, K. C. Atmospheric pressure chemical vapor deposition of tin sulfides (SnS, Sn_2S_3, and SnS_2) on glass. *Chem. Mater.* **1999**, *11*, 1792–1799.

[3] Rajeshwar, K.; de Tacconi, N. R.; Chenthamarakshan, C. R. Semiconductor-based composite materials: Preparation, properties, and performance. *Chem. Mater.* **2001**, *13*, 2765–2782.

[4] Chen, D.; Shen, G. Z.; Tang, K. B.; Lei, S. J.; Zheng, H. G.; Qian, Y. T. Microwave-assisted polyol synthesis of nanoscale SnS_x [x = 1, 2] flakes. *J. Cryst. Growth* **2004**, *260*, 469–474.

[5] Nassary, M. M. Temperature dependence of the electrical conductivity, Hall effect and thermoelectric power of SnS single crystals. *J. Alloy Compd.* **2005**, *398*, 21–25.

[6] Boonsalee, S.; Gudavarthy, R. V.; Bohannan, E. W.; Switzer, J. A. Epitaxial electrodeposition of tin(II) sulfide nanodisks on single-crystal Au(100). *Chem. Mater.* **2008**, *20*, 5737–5742.

[7] Hayashi, A.; Konishi, T.; Tadanaga, K.; Minami, T.; Tatsumisago, M. All-solid-state lithium secondary batteries with SnS–P_2S_5 negative electrodes and Li_2S–P_2S_5 solid electrolytes. *J. Power Sources* **2005**, *146*, 496–500.

[8] Li, Y.; Tu, J. P.; Huang, X. H.; Wu, H. M.; Yuan, Y. F. Nanoscale SnS with and without carbon-coatings as an anode material for lithium ion batteries. *Electrochim. Acta* **2006**, *52*, 1383–1389.

[9] Li, Y.; Tu, J. P.; Huang, X. H.; Wu, H. M.; Yuan, Y. F. Net-like SnS/carbon nanocomposite film anode material for lithium ion batteries. *Electrochem. Commun.* **2007**, *9*, 49–53.

[10] Aso, K.; Hayashi, A.; Tatsumisago, M. Synthesis of needlelike and platelike SnS active materials in high-boiling solvents and their application to all-solid-state lithium secondary batteries. *Cryst. Growth Des.* **2011**, *11*, 3900–3904.

[11] Zhang, Y. J.; Lu, J.; Shen, S. L.; Xu, H. R.; Wang, Q. B. Ultralarge single crystal SnS rectangular nanosheets. *Chem. Commun.* **2011**, *47*, 5226–5228.

[12] Hegde, S. S.; Kunjomana, A. G.; Chandrasekharan, K. A.; Ramesh, K.; Prashantha, M. Optical and electrical properties of SnS semiconductor crystals grown by physical vapor deposition technique. *Physica B* **2011**, *406*, 1143–1148.

[13] Yang, J.; Winter, M.; Besenhard, J. O. Small particle size multiphase Li-alloy anodes for lithium-ion-batteries. *Solid State Ionics* **1996**, *90*, 281–287.

[14] Gou, X. L.; Chen, J.; Shen, P. W. Synthesis, characterization and application of SnS_x (x = 1, 2) nanoparticles. *Mater. Chem. Phys.* **2005**, *93*, 557–566.

[15] Park, M. S.; Wang, G. X.; Kang, Y. M.; Wexler, D.; Dou, S. X.; Liu, H. K. Preparation and electrochemical properties of SnO_2 nanowires for application in lithium-ion batteries. *Angew. Chem. Int. Ed.* **2007**, *46*, 750–753.

[16] Chan, C. K.; Peng, H.; Liu, G.; McIlwrath, K.; Zhang, X. F.; Huggins, R. A.; Cui, Y. High-performance lithium battery anodes using silicon nanowires. *Nat. Nanotechnol.* **2008**, *3*, 31–35.

[17] Wang, Z.; Luan, D.; Madhavi, S.; Li, M. C.; Lou, W. X. α-Fe_2O_3 nanotubes with superior lithium storage capability. *Chem. Commun.* **2011**, *47*, 8061–8063.

[18] Kim, D. K.; Muralidharan, P.; Lee, H. W.; Ruffo, R.; Yang, Y.; Chan, C. K.; Peng, H.; Huggins, R. A.; Cui, Y. Spinel $LiMn_2O_4$ nanorods as lithium ion battery cathodes. *Nano Lett.* **2008**, *8*, 3948–3952.

[19] Kim, M. G.; Jo, M.; Hong, Y.-S.; Cho, J. Template-free synthesis of $Li[Ni_{0.25}Li_{0.15}Mn_{0.6}]O_2$ nanowires for high performance lithium battery cathode. *Chem. Commun.* **2009**, 218–220.

[20] Lim, S. Y.; Yoon, C. S.; Cho, J. P. Synthesis of nanowire and hollow $LiFePO_4$ cathodes for high-performance lithium batteries. *Chem. Mater.* **2008**, *20*, 4560–4564.

[21] Li, X. X.; Cheng, F. Y.; Guo, B.; Chen, J. Template-synthesized $LiCoO_2$, $LiMn_2O_4$, and $LiNi_{0.8}Co_{0.2}O_2$ nanotubes as the cathode materials of lithium ion batteries. *J. Phys. Chem. B* **2005**, *109*, 14017–14024.

[22] Liu, J.; Xue, D. Sn-based nanomaterials converted from SnS nanobelts: Facile synthesis, characterizations, optical properties and energy storage performances. *Electrochim. Acta* **2010**, *56*, 243–250.

[23] Panda, S. K.; Datta, A.; Dev, A.; Gorai, S.; Chaudhuri, S. Surfactant-assisted synthesis of SnS nanowires grown on tin foils. *Cryst. Growth Des.* **2006**, *6*, 2177–2181.

[24] Biswas, S.; Kar, S.; Chaudhuri, S. Thioglycolic acid (TGA) assisted hydrothermal synthesis of SnS nanorods and nanosheets. *Appl. Surf. Sci.* **2007**, *253*, 9259–9266.

[25] Dhanaraj, G.; Byrappa, K.; Prasad, V.; Dudley, M. *Springer Handbook of Crystal Growth*; Springer-Verlag: Berlin Heidelberg, **2010**.

[26] Francis, R. J.; Price, S. J.; Evans, J. S. O.; O'Brien, S.; O'Hare, D.; Clark, S. M. Hydrothermal synthesis of microporous tin

sulfides studied by real-time *in situ* energy-dispersive X-ray diffraction. *Chem. Mater.* **1996**, *8*, 2102–2108.

[27] Mariano, A. N.; Chopra, K. L. Polymorphism in some Ⅳ–Ⅳ compounds induced by high pressure and thin-film epitaxial growth. *Appl. Phys. Lett.* **1967**, *10*, 282–284.

[28] Kim, D.; Shimpi, P.; Gao, P. X. Zigzag zinc blende ZnS nanowires: Large scale synthesis and their structure evolution induced by electron irradiation. *Nano Res.* **2009**, *2*, 966–974.

[29] Hickey, S. G.; Waurisch, C.; Rellinghaus, B.; Eychmuller, A. Size and shape control of colloidally synthesized Ⅳ–Ⅵ nanoparticulate tin(Ⅱ) sulfide. *J. Am. Chem. Soc.* **2008**, *130*, 14978–14980.

[30] Tanusevski, A. Optical and photoelectric properties of SnS thin films prepared by chemical bath deposition. *Semicond. Sci. Technol.* **2003**, *18*, 501–505.

[31] Liu, H. T.; Liu, Y.; Wang, Z.; He, P. Facile synthesis of monodisperse, size-tunable SnS nanoparticles potentially for solar cell energy conversion. *Nanotechnology* **2010**, *21*, 105707.

[32] Seo, J. W.; Jang, J. T.; Park, S. W.; Kim, C. J.; Park, B. W.; Cheon, J. W. Two-dimensional SnS_2 nanoplates with extraordinary high discharge capacity for lithium ion batteries. *Adv. Mater.* **2008**, *20*, 4269–4273.

[33] Zhang, W.-M.; Hu, J.-S.; Guo, Y.-G.; Zheng, S.-F.; Zhong, L.-S; Song, W.-G.; Wan, L.-J. Tin-nanoparticles encapsulated in elastic hollow carbon spheres for high-performance anode material in lithium-ion batteries. *Adv. Mater.* **2008**, *20*, 1160–1165.

[34] Liu, S.; Yin, X. M.; Chen, L. B.; Li, Q. H.; Wang, T. H. Synthesis of self-assembled 3D flowerlike SnS_2 nanostructures with enhanced lithium ion storage property. *Solid State Sci.* **2010**, *12*, 712–718.

[35] Huggins, R. A. Lithium alloy negative electrodes. *J. Power Sources* **1999**, *81–82*, 13–19.

[36] Idota, Y.; Kubota, T.; Matsufuji, A.; Maekawa, Y.; Miyasaka, T. Tin-based amorphous oxide: A high-capacity lithium-ion-storage material. *Science* **1997**, *276*, 1395–1397.

[37] Besenhard, J. O. *Handbook of Battery Materials*; Wiley-VCH: Weinheim, **1999**.

[38] Courtney, I. A.; Dahn, J. R. Key factors controlling the reversibility of the reaction of lithium with SnO_2 and Sn_2BPO_6 glass. *J. Electrochem. Soc.* **1997**, *144*, 2943–2948.

[39] Lou, X. W.; Wang, Y.; Yuan, C.; Lee, J. Y.; Archer, L. A. Template-free synthesis of SnO_2 hollow nanostructures with high lithium storage capacity. *Adv. Mater.* **2006**, *18*, 2325–2329.